American Mineralogist, Volume 93, pages 533–539, 2008

Possible structural polymorphism in Al-bearing magnesiumsilicate post-perovskite†

Oliver Tschauner,[1,2,*] Boris Kiefer,[3] Haozhe Liu,[4,5] Stanislas Sinogeikin,[4] Maddury Somayazulu,[4,6] and Sheng-Nian Luo[7]

[1]High Pressure Science and Engineering Center, Department of Physics, University of Nevada, Las Vegas, Nevada 89154, U.S.A.
[2]Division of Geology and Planetary Sciences, California Institute of Technology, Pasadena, California 91125, U.S.A.
[3]Department of Physics, New Mexico State University, Las Cruces, New Mexico 88003, U.S.A.
[4]HPCAT, Advanced Photon Source, Argonne National Laboratory, Argonne, Illinois 60439, U.S.A.
[5]Center for Condensed Matter Science and Technology, Research Academy of Science and Technology, Harbin 150080, China
[6]Geophysical Laboratory, Carnegie Institution of Washington, Washington, D.C. 20015, U.S.A.
[7]Physics Division, Los Alamos National Laboratory, Los Alamos, New Mexico 87545, U.S.A.

Abstract

In the present study, we summarize indications for the existence of kinked post-perovskite structures in the MAS system. X-ray diffraction data and Raman spectra of aluminous magnesium metasilicate post-perovskite are inconsistent with the $CaIrO_3$ structure. Instead the observations are consistent with structures intermediate between the perovskite and the $CaIrO_3$ structure. Ab initio calculations show that the enthalpies of the kinked structures are slightly higher than the $CaIrO_3$ structure at 0 K. Finite temperature, minor element chemistry, kinetics of phase transformation, and actual stress regime are plausible reasons for the observed differences between the present and the previously reported post-perovskite phases.

Keywords: Crystal structure, post-perovskite, XRD data, quantum mechanical calculation, high-pressure studies, Raman spectroscopy

Introduction

The major phase of the Earth's lower mantle is magnesium metasilicate in the perovskite structure. Recently, a first-order phase transformation of this silicate-perovskite into a phase with quite different structure was proposed based on experiments at pressures and temperatures of the lowermost mantle (Murakami et al. 2004; Oganov and Ono 2004). Furthermore, first-principles calculations indicate that the $CaIrO_3$-type structure of $MgSiO_3$ is more stable than the perovskite structure at the pressures of the core-mantle boundary region at 0 K (Oganov and Ono 2004; Tsuchiya et al. 2004a). Moreover, the Clapeyron-slope of the pervoskite-to-post-perovskite phase transition has been calculated to be positive and of a magnitude that makes existence of post-perovskite in colder regions of the deepest mantle likely (Oganov and Ono 2004; Tsuchiya et al. 2004b). This discovery has the potential to change our understanding of this important region in the Earth. Marked differences in thermoelastic properties between magnesium silicate perovskite and post-perovskite may account for anomalous seismic features in the lowermost mantle. For example, the positive Clapeyron slope of the phase boundary may control size and number of plumes forming in this region of the Earth (Nakagawa and Tackley 2004; Helmberger et al. 2005; Kameyama and Yuen 2006). It is of most interest to determine the influence of minor element chemistry and the actual stress-temperature regime on the structure of post-perovskite and to examine if there are intermediates between perovskite and the reported post-perovskite phase. The observation of unexplained diffraction features in perovskite-post-perovskite assemblies synthesized from pyrope at 140 GPa (Tateno et al. 2005) may be an indication that structural intermediates occur as stable or metastable phases for mixed compositions in the magnesium-aluminum-silicate (MAS) system. Recently, Oganov et al. (2005) proposed a new type of kinked post-perovskite structures that are intermediate between perovskite and $CaIrO_3$-post-perovskite. Here, we present ab initio calculations, X-ray diffraction data, and Raman spectra that support the formation of such kinked post-perovskite structures in aluminous and ferrous aluminous magnesium metasilicate.

Theory

To assess the stability of the proposed structures we performed ab-initio calculations with the Vienna Ab-initio software package (Kresse and Hafner 1993; Kresse and Furthmüller 1996) for $MgSiO_3$ post-perovskite. The calculations are based on density-functional theory (Hohenberg and Kohn 1964). Electronic correlations were treated with the GGA in the parameterization of Perdew et al. (1996). We used PAW potentials (Blöchl 1994; Kresse and Joubert 1999) for Mg (valence states $3s^2$), Si ($3s^22p^4$), and O ($2s^22p^4$) with core radii of 2.000 a_B, 1.508 a_B, and 1.525 a_B for Mg, Si, and O, respectively. The calculations for $MgSiO_3$-perovskite and $MgSiO_3$-post-perovskite were performed using 6 × 6 × 4 and 6 × 4 × 6 k-point grids (Monkhorst and Pack 1976), respectively. All calculations for the intermediate structures were performed using a 1 × 2 × 2 k-point grid. An energy cut-off of 600 eV was sufficient to converge energies to within 1 meV per $MgSiO_3$ unit and pressures to within 0.3 GPa. All calculations were performed in symmetry preserving mode at static condi-

* E-mail: olivert@physics.unlv.edu

† Open Access: Thanks to the authors' generous funding this article is available to all online (http://ammin.geoscienceworld.org) and the MSA web site, which also has information about the MSA Open Access policy at http://www.minsocam.org/MSA/ammin/e-pub_policy.htm (scroll down).

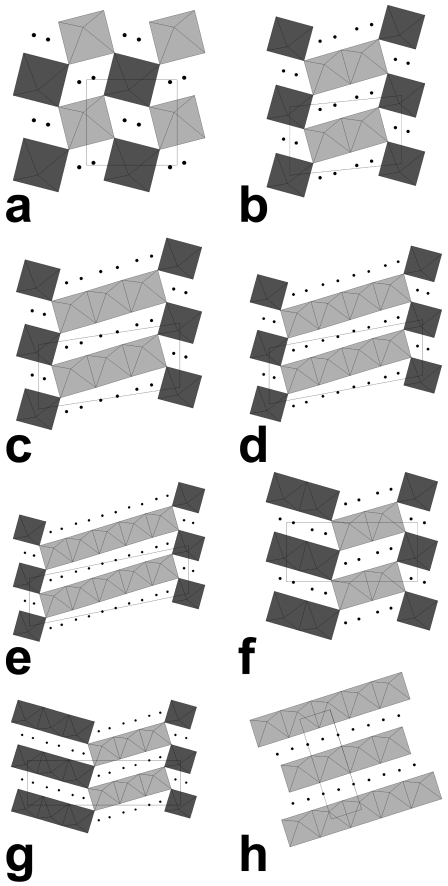

FIGURE 1. View along the [001] direction of the relaxed structures from the ab initio calculations. The two types of layers are indicated by light and dark shading of the SiO_6-octahedra in each layer. Magnesium atoms are shown as black circles and unit cells are indicated by thin solid lines. (**a**) 1 × 1 (perovskite); (**b**) 2 × 1; (**c**) 3 × 1; (**d**) 4 × 1; (**e**) 5 × 1; (**f**) 2 × 2; (**g**) 3 × 3; (**h**) ∞ × 0 ($CaIrO_3$). We also give the calculated fractional coordinates of the 2 × 1 and the 3 × 1 type structures as they are used to model the observed diffraction patterns.

2 × 1: Mg: 0.057, ¼, 0.538; 0.269, ¾, 0.083; 0.730, ¼, 0.917; Si: 0, 0, 0; 0.330, 0.502, 0.555; 0.380, ¼, 0.820; O: 0.792, 0.560, 0.140; 0.207, 0.060, 0.860; 0.306, ¼, 0.429; 0.458, 0.555, 0.243; 0.644, ¼, 0.313.

3 × 1: Mg: 0.042, ¼, 0.514; 0.303, ¼, 0.073; 0.559, ¼, 0.989; 0.799, ¼, 0.895; Si: 0, 0, 0; ½, 0, ½; 0.247, 0.501, 0.583; O: 0.985, ¼, 0.111; 0.230, ¼, 0.455; 0.480, ¼, 0.368; 0.7352, ¼, 0.287; 0.845, 0.559, 0.125; 0.906, 0.443, 0.647; 0.343, 0.556, 0.283; 0.407, 0.444, 0.801.

tions (0 K). The initial model post-perovskite structures were generated as follows: The perovskite structure if viewed along [001] can be described as the stacking of two types of "layers" (A and B) with sequence ...BABABA... running in [010] direction (Fig. 1a). Polytypes with different layer sequences were generated by inserting layers into the perovskite structure such that a continuous SiO_6 network was maintained (Figs. 1b–1g). We adopt the nomenclature for different stacking sequences from Oganov et al. (2005): n × m represents a sequence with n, m sequential layers of type A and type B, respectively. If only A layers are added the resulting n × 1 and n × m structures all belong to space group $P2_1/m$ (Table 1). Similarly, structures of type n × n belong to space group *Pbnm*. The 2 × 2 and the 3 × 1

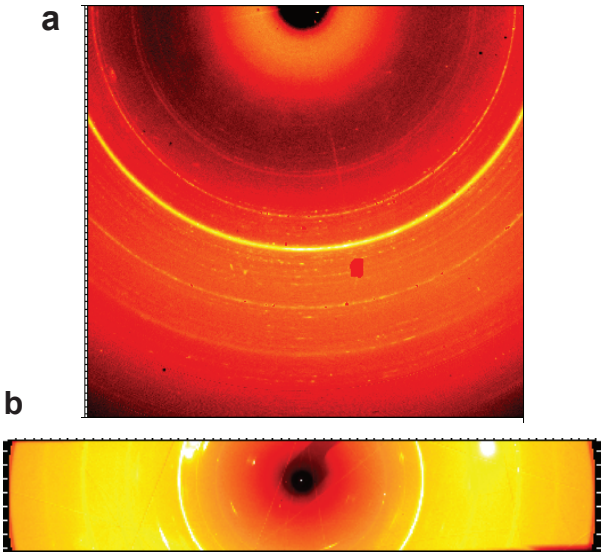

FIGURE 2. (**a**) Diffraction patterns from Sample 2 at 93 GPa. The diffraction is from the KBr pressure medium, from $MgSiO_3$-perovskite, and from post-perovskite-like material. In any case, the diffraction features are Debye fringes from a powdered material with minor granularity. (**b**) Sample 1 at 115 GPa. This sample exhibits noticeable texture in a fine-grained sample aggregate. The intensity distribution is therefore not homogeneous along each Debye fringe but modulated. Another obvious consequence of texture is the alternating sequence of sections of enhanced and oppressed diffraction intensity along the sequence of 2θ angles of observed diffraction.

structure have been described previously (Oganov et al. 2005). Inserting more A type layers increases the length of the edge sharing chains relative to the corner sharing Si-octahedra (Figs. 1d–1g) and the post-perovskite phase is obtained in the limit of infinite chain length. Structures of type 1 × 1 (perovskite), 2 × 2, 3 × 3, 2 × 1, 3 × 1, 4 × 1, 5 × 1, 6 × 1, 4 × 3, and (∞,0 – $CaIrO_3$-type) were relaxed to explore their relative energies and crystal chemistry and as initial structure models for the interpretation of the experimental diffraction data.

We considered different stacking sequences of the A and B layers. We find that all these kinked structures are energetically comparable to the $CaIrO_3$-type post-perovskite phase for $MgSiO_3$ (Table 2). However, the results show that the $CaIrO_3$-type phase still has the lowest enthalpy at 0 K.

EXPERIMENTAL METHODS

Planar single-crystal chips of pristine orthopyroxene and of gedrite were selected and analyzed with a JEOL JXA-8900 electron microprobe operated at 15 kV accelerating voltage and 8 nA current. The orthopyroxene sample was a crystal of gem quality from Sri Lanka, (Si: 1.984 ± 0.003, Al: 0.060 ± 0.001, Ti: 0.001 ± 0.000, Fe: 0.010 ± 0.001, Mg: 1.924 ± 0.005, Ca: 0.004 ± 0.000), the gedrite was from an unknown locality (Si: 10.993 ± 0.006, Al: 1.02 ± 0.18, Fe: 2.27 ± 0.46, Mg: 5.81 ± 0.82, Na: 0.62 ± 0.09). The samples were loaded in Mao-Bell type and symmetric diamond anvil cells with Re-gaskets as pressure-transmitting media. The samples were completely surrounded by NaCl (Sample 1) or KBr (Sample 2). The volume ratio sample to alkali halide was about 1:4 (NaCl) and 1:7 (KBr). The alkali halide served as a pressure-transmitting and heat-insulating medium with the prospect of providing conditions of low deviatoric stress during the experiment. Sample 1 contained orthopyroxene and NaCl plus two small spherules of ruby; Sample 2 contained gedrite, KBr, platinum, and one spherule of ruby. All samples were annealed at all pressures to reduce stress gradients during heating.

The beams of two CO_2-lasers were focused simultaneously onto the pressurized silicate samples. The sample assembly allowed for several independent determinations of pressure: (1) spherules of ruby of 3–5 μm diameter, (2) the insulating medium itself; and (3) platinum.

In the first set of experiments (Sample 1), we changed the pressure several times between 100 and 120 GPa and heated at each pressure point to homogenize the stress conditions in the sample. In detail the loading and heating cycles during the first experiment were as follows: Initially, the sample was pressurized to 80 GPa and heated to ~ 2000 K for 300 s to convert the orthopyroxene sample to the perovskite structure. Then the sample was pressurized to between 110 and 120 GPa and heated to 2200 (±100) K for 600 s. The pressure after heating was 105 ± 5 GPa. Because ruby was incidentally heated by the laser beam upon alignment and underwent a structural transition upon heating (Lin et al. 2004), we used the volume of NaCl to calculate the pressure (Fei et al. 2007; Sata et al. 2002) and the given uncertainties are from the combined error in volume determination and in calibration of the NaCl-scale relative to the Pt-scale (Sata et al. 2002) and to the gold scale (Fei et al. 2007). The volume was obtained upon Rietveld refinement of the NaCl structure using the experimental diffraction pattern ($R_{F^2} = 0.04$). While there is no absolute calibration of pressure at 100 GPa better than ±10 GPa (Holzapfel 2003), the volume of NaCl will allow for more accurate determination of pressure once a better pressure scale is established. Thereafter, we reduced and raised pressure between 98 and 115 ± 3 GPa two further times and heated the sample each time to 2000–2200 K.

In the second experiment (Sample 2) we raised the pressure initially to 80 GPa based on ruby fluorescence (Mao et al. 1990) and heated the sample for 300 s to 1800 K. At this pressure and temperature perovskite is the stable structure, and it is known that this phase has very limited solubility of water (Bolfan-Casanova et al. 2003; Ross et al. 2003). We assume that the water of the gedrite starting material has been mostly removed during this heating. Afterward, we raised the pressure to around 100 GPa and heated the sample to 2200 ± 50 K for 380 s. Diffraction data were collected after reducing temperature to 300 K, and the pressure was found to be 93 ± 2 GPa from the platinum pressure marker (Fei et al. 2007) and 95.0 ± 1 GPa from ruby (Mao et al. 1990).

X-ray diffraction patterns were collected at the 16ID-B undulator beamline at the High Pressure Collaborative Access Team (HPCAT), section 16 of the APS-ANL synchrotron, using a monochromatic beam of 32 or 36 keV energy focused with Kirkpatrick-Baez mirrors to 10 × 14 μm² and a Mar345 image plate detector. We integrated the diffraction images and corrected for geometric distortions using the Fit2D software package (Hammersley et al. 1996).

Raman spectra were collected immediately after the diffraction experiment using the micro-Raman spectrometer of GSECARS at Sector 13 of the APS-ANL synchrotron operated with the 514.5 nm excitation line of an Ar-ion laser at 60 mW power focused to a spot of about 10 μm diameter in 180° backscattering geometry, a Spex 0.5 m monochromator with a single 1200 grooves/mm grating, 20 μm slit-width, and a liquid nitrogen cooled CCD camera detector from Oxford Instruments. We collected spectra at different locations of the silicate sample and in the pressure medium. There is no variation of the spectral features in the sample while the medium does not yield any Raman signal even at a distance of one diameter of the laser focal spot from the silicate. The recorded Raman spectra therefore belong to the silicate samples.

TABLE 1. Comparison of space groups, cell parameters, unit-cell volume of various kinked post-perovskite type phases for fixed atomic volume of 6.185 Å³

Structure	*P* (GPa)	*V* (Å³)	*a* × *b* × *c* (Å)			β (°)
Pv, *Pbnm*	124.9	123.7	4.583	6.282	4.295	90
2 × 1, $P2_1/m$	120.4	185.5	7.026	6.228	4.262	95.85
3 × 1, $P2_1/m$	118.7	247.4	9.477	6.205	4.256	98.75
4 × 1, $P2_1/m$	117.9	309.2	11.937	6.191	4.255	100.45
5 × 1, $P2_1/m$	117.3	371.0	14.403	6.182	4.253	101.57
6 × 1, $P2_1/m$		432.7	16.275	6.266	4.311	101
2 × 2, *Pnma*	118.5	247.4	9.368	6.209	4.253	90
3 × 3, *Pnma*	117.0	371.0	14.122	6.185	4.248	90
4 × 3, $P2_1/m$	116.7	432.9	16.507	6.179	4.248	92.51
$CaIrO_3$, *Cmcm*	115.4	123.7	2.476	8.127	6.145	90

RESULTS AND DISCUSSION

Figure 2 shows the diffraction images of Samples 1 and 2 at 115 and 93 GPa, respectively. These images correspond to the integrated patterns shown in Figure 3a and 3b. Sample 2 exhibits a fine-spaced sequence of narrow, smooth, and continuous Debye-fringes (Fig. 2a), while Sample 1 exhibits marked texture (Fig. 2b). We discuss the data of Sample 2 first. We calculated the diffraction patterns of silicate perovskite, $CaIrO_3$-post-perovskite, and kinked post-perovskite structures (Table 2) and compared them to the observed patterns (Fig. 3a).

In the case of Sample 2 (no texture), we used the Rietveld refinement method to quantify and optimize the match between calculated and observed diffraction pattern adjusting profile

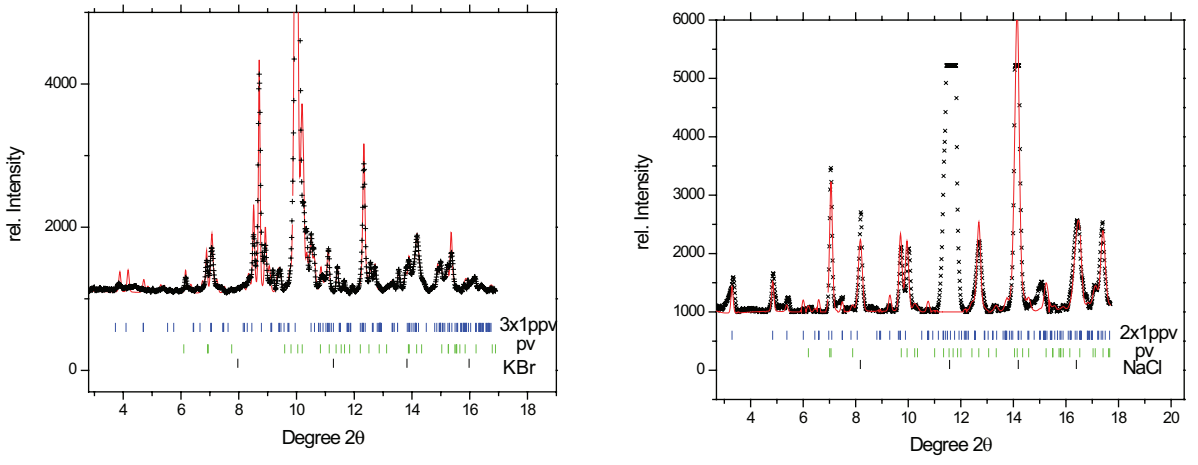

FIGURE 3. Rietveld refinements of the integrated diffraction patterns from Samples 1 and 2. Black crosses = Observed signal; red line = modeled diffraction pattern; tick marks = 2θ-angles of observed reflections. (**a**) Sample 2: wavelength was 0.34531 Å. The whole pattern, including background (not shown here) was fitted. For $MgSiO_3$-perovskite we find an R_{F^2} of 0.09, for the 3 × 1 kinked post-perovskite R_{F^2} is 0.24, and for KBr 0.04. The fitted cell parameters of the 3 × 1 phase are 9.608(16) × 6.043(13) × 4.248(8) Å³, β = 98.689(14)°, the cell parameters of pervoskite are 4.442(1) × 4.651(1) × 6.438(1) Å³, and the cell parameter for KBr is 2.7979(3) Å. The standard deviation is given in brackets. (**b**) Sample 1: wavelength was 0.3888 Å. Background was subtracted in advance of Rietveld refinement because of a strong modulation from excitation halos around the intense peaks for the pressure medium. The weighted profile refinement parameter wRp was 0.09 and $\chi^2 = 31.3$. The R_{F^2} for the 2 × 1 phase was 0.25. The cell parameters are 6.804(5) × 6.289(7) × 4.161(4) Å³, β = 96.17(9)°. The cell parameter for NaCl is 2.727(1) Å and for perovskite 4.445(3) × 4.598(4) × 6.372(3) Å³.

parameters, background, and, finally, optimizing the structure models. We used the profile-weighted agreement factor R_{wp} of 0.018 and a χ^2 of 14.5. More importantly, this fit gives a R_{F2} of 0.09 for the silicate-perovskite (Fig. 3a). This small value shows that the F-factor weighted profile refinement is not artificially convergent but corresponds to a meaningful extraction of $|F|^2$ of perovskite from the fitted profiles. This good fit of the perovskite pattern also shows that there are diffraction features that do not belong to perovskite. We compare these diffraction features to the calculated pattern of $CaIrO_3$-post-perovskite, Al_2O_3 in the high-pressure structure (Lin et al. 2004), and several of the proposed kinked post-perovskite phases as listed in Table 1. Although the $CaIrO_3$-type and Al_2O_3 do not match the diffraction pattern or any part of it, kinked phases show clearly better matching and a best match is achieved for the 3×1 type phase (Table 1; Fig. 3a). The overall correspondence of observed Bragg angles and predicted reflection angles is good. The observed X-ray peaks at 2θ angles between 3.5 and 5.5° indicates the existence of diffraction planes in the sample assembly that can neither be explained by perovskite nor by $CaIrO_3$ type—post-perovskite or alumina. In contrast, kinked structures (with larger unit cells) allow for matching of these two low angle peaks. We note that marked diffraction at such low angles have been observed by Tateno et al. (2005) in the patterns of mixed perovskite and post-perovskite assemblies from laser heating experiments. Marked peaks at 12.8° and between 13 and 13.9 °2θ do not correspond to reflections of perovskite but are matched by predicted peaks of the 3×1 type structure and even peaks of low intensity seem to match weaker features in the observed pattern. Subsequent Rietveld refinement (Fig. 3a) converges to an R_{F2} of 0.24. This level of matching between observed and calculated structure factor moduli suggests that the observed pattern belongs to a phase of at least structural similarity to the 3×1 kinked phase but it certainly leaves freedom for structural variations. For comparison, $CaIrO_3$-type post-perovskite yields a R_{F2} of about 0.8 with the same pattern and profile parameters.

Because of the rather large instrumental contribution and the complex background in our data R_{wp} is not a good measure for judging the validity of a structure model. On the other hand, the modeled silicate structures are of low symmetry and strict overlap of reflections is not significant. Therefore, R_{F2} is a more trustworthy measure of the proximity between the modeled structures and the observation than R_{wp} in the present case.

In summary, the X-ray diffraction pattern in Figure 3a shows features in ferrous aluminous $MgSiO_3$ at 91–95 GPa that cannot be explained by perovskite, $CaIrO_3$ type post-perovskite, or alumina. In contrast an intermediate 3×1 kinked post-perovskite structure provides a more consistent interpretation of the unexplained diffraction features especially at low 2θ angles. The remaining mismatch between observed and predicted structure factors may be due to several reasons: The total fraction of the new phase is only a third of the fraction of perovskite. Thus, refinement based on whole profile fitting is more sensitive to slight mismatches in background and profiles of coexisting phases and this affects extraction of $|F|^2$ values. Furthermore, the diffraction peaks show variable width and this, again, is difficult to fit if the signal to noise ratio is not very high. Finally it is possible that the observed pattern actually belongs to a mixture of similar kinked post-perovskite structures although we can preclude presence of alumina as free phase (see above).

The diffraction image of Sample 1 indicates noticeable texture of a fine-grained polycrystalline aggregate (Fig. 2b). After integration we ran an automatic indexing of the observed sample Bragg peaks using the Jade 7.5+ package. To our surprise, we found a small number of orthorhombic and monoclinic cells of mostly equal cell dimensions, volumes, and angle. This suggests that the observed peaks belong to a single phase. We examined these candidate cells with respect to $CaIrO_3$-type post-perovskite, our calculated post-perovskite polymorphs, and perovskite. The diffraction data from the present experiment are clearly different from perovskite and $CaIrO_3$-type post-perovskite (Table 1). However, all observed reflections including 12 distinct reflections below 12 °2θ, can be indexed by the cell of the 2×1 type post-perovskite structure with dimensions $6.76 \times 6.32 \times 4.65$, $\beta = 99.2°$, which is similar to the cell of the 2×1 structure as obtained from the ab initio calculations for pure $MgSiO_3$ (Table 1).

We calculated the powder diffraction pattern of 2×1 kinked post-perovskite based on the atomic positions of the ab-initio calculated structure and compared it to the observed pattern. Subsequent Rietveld refinement focuses on matching the apparent texture by spherical harmonics up to second order (Fig. 3b) using the method by von Dreele (1997). Along with the profile weighted refinement parameters (see caption Fig. 3b) this procedure shows a match of calculated and observed structure factor moduli of an R_{F2} of 0.25. As for Sample 1, we find that the diffraction pattern of this sample is incompatible with perovskite, $CaIrO_3$-type post-perovskite, and alumina, while the observed pattern in this case is consistent with a 2×1 kinked post-perovskite. Both Samples 1 and 2 show well-resolved low angle diffraction peaks in the range of 3.5 to 6 in °2θ. This observation is incompatible with perovskite and $CaIrO_3$-type post-perovskite while it is consistent with kinked post-perovskite.

TABLE 2. Comparison of energies and equation-of-state parameters of perovskite, kinked structures, and $CaIrO_3$-type post-perovskite

Structure	ΔE_0 (eV/20 atoms)	V_0 (Å^3/20 atoms)	K_0 (GPa)	K_0' (–)	ΔH (Ev/20 atoms)
Pv	0 (0)	166.9 (168.0)	232.6 (230.9)	3.93 (4.13)	(0)
2×1	0.675	168.5	205.1	4.17	0.422
3×1	0.706 (0.645)	168.5 (169.6)	196.6 (198.6)	4.34 (4.52)	0.199 (0.240)
4×1	0.759	168.4	194.2	4.40	0.101
5×1	0.804	168.2	193.6	4.43	0.042
6×1	0.834	168.1	193.9	4.42	0.009
2×2	0.696 (0.685)	169.1 (170.1)	191.3 (194.0)	4.38 (4.55)	0.266 (0.353)
3×3	0.852	169.0	184.6	4.56	0.142
4×3	0.886	168.7	186.5	4.53	0.167
$CaIrO_3$	0.916 (0.928)	167.2 (168.2)	201.0 (201.8)	4.29 (4.50)	–0.174 (–0.148)

Notes: Enthalpy differences (ΔH) at a pressure of 115 GPa are relative to perovskite. Extensive quantities are per 20 atoms. In the present study, a third-order Birch-Murnaghan equation of state was fitted. In Oganov et al. 2005, a Vinet equation of state was used. Available results from Oganov et al. (2005) are shown in parentheses.

Upon subsequent extended heating cycles of Sample 1 (see experimental section) the size of crystallites increased, and the diffraction pattern changes from that of a textured powder to that of a few larger crystallites that give rise to several individual Bragg reflections at different locations of the image plate detector. The textural pattern shows that during the high *P-T* experiment the silicate sample had passed from a regime of formation of randomly oriented crystalline seeds into a regime of collective recrystallization and re-orientation. This state is the result of repetitive heating under conditions of small temperature gradients, due to the use of a comparatively thick envelope of pressure medium of apparently lower thermal conductivity than the sample itself (Kiefer and Duffy 2005) and due to direct heating of the silicate sample rather than using mixed-in metallic absorbers. We observe 52 reflections that belong to various crystallites. Out of this set we select seven reflections which seem to belong to one crystallite since they establish two intersecting lattice trajectories which can be mapped onto each other (Fig. 1 Appendix). Because our diffraction patterns were collected at a fixed angular position, we sample only a two-dimensional slice of the reciprocal space. It is the narrow backside aperture of the Mao-Bell cell that does not permit sampling of further angular settings. Because of the two-dimensionality of the observable portion of reciprocal space we are constrained to compare the 2θ angles of these reflections to silicate-perovskite, $CaIrO_3$-post-perovskite, and the kinked post-perovskite structures (Table 1 Appendix). This comparison is presented in table 1 of the Appendix. It shows consistence of the observed set of 2θ values with various n × 1 type kinked post-perovskites while it is inconsistent with either perovskite or $CaIrO_3$-type post-perovskite. This is discussed in more detail in the Appendix.

Raman spectra

We collected Raman spectra from Samples 1 and 2 directly after collection of the diffraction data and at the same pressure. Figure 4, upper part, shows the Raman spectrum of Sample 2 (powder), at a pressure after heating of 93 ± 3 GPa. A shoulder at 750 cm^{-1} and weaker features at 380 and 495 cm^{-1} match the Raman shifts of silicate-perovskite at this pressure regime (Serghiou et al. 1998) that is not unexpected since perovskite was also identified in the corresponding diffraction pattern. However, several other well resolved peaks in this spectrum cannot be assigned to perovskite (Table 3), in particular we observe a strong broad, structured, peak between 750 and 1000 cm^{-1}. According to previous experimental (Serghiou et al. 1998) and computational studies (Karki et al. 2000; Caracas and Cohen 2006), no Raman active modes are expected for $MgSiO_3$-perovskite in this energy range. On the other hand, Caracas and Cohen (2006) predicted the occurrence of Raman active modes in this energy range at comparable pressures (120 GPa) for the $CaIrO_3$-type post-perovskite phase of $MgSiO_3$.

It is interesting to compare the Raman spectrum in Figure 4, upper part, to the calculated spectrum of $CaIrO_3$-type magnesium silicate post-perovskite (Caracas and Cohen 2006). In both cases, the spectrum is dominated by a high energy peak which conceivably receives intensity from modes involving Si-O octahedral stretching vibrations that are Raman inactive in the perovskite structure but are Raman active in the $CaIrO_3$-type phase (Caracas and Cohen 2006). Since the kinked post-perovskite structures are of lower symmetry than the $CaIrO_3$-type phase and have larger unit cells many of these vibrations involving Si-O octahedral stretching motions remain active in kinked post-perovskite structures.

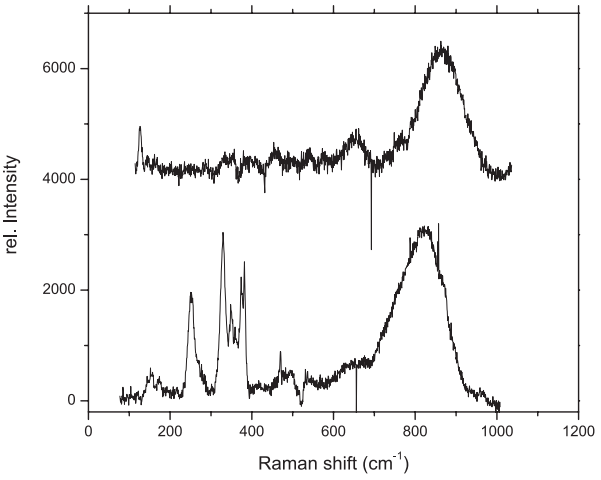

Figure 4. Raman spectra of the two samples at the pressures of 95 and 115 GPa. The Raman spectra were collected right after the diffraction experiment without changing pressure or additional heating. Both spectra are dominated by Raman peaks above 700 cm^{-1} where perovskite does not have measurable Raman scattering intensity (Serghiou et al. 1998; Karki et al. 2002). These strong features are not single broad peaks but are composed of several overlapping peaks which appear as shoulders in the spectra, in particular in the spectrum of Sample 1 (lower spectrum). The lower frequency part of the spectrum is complex and involves more Raman peaks than expected for the $CaIrO_3$-type structure (see text). Sample 1 (lower spectrum) exhibits marked texture (Fig. 2b) and the observed Raman peak intensities are not expected to represent an average. The upper spectrum (Sample 2) is from a powdered sample.

Figure 4, lower part, shows the Raman spectrum of Sample 1 (textured) at 115 ± 5 GPa. The spectrum also shows a strong broad, structured peak between 700 and 1000 cm^{-1} while there are sharp and intense peaks between 250 and 500 cm^{-1}. For this textured sample intensities are likely controlled by crystallite orientation (see Figs. 2b and 3b caption), while the spectrum of Sample 2 gives an average over a powder.

Sample 1 shows at least 22 Raman peaks (Table 3) none of which adheres to perovskite, whereas the $CaIrO_3$-structure exhibits only 12 Raman active modes according to the Bilbao Crystallographic Server (Kroumova et al. 2003). The broad peaks between 700 and 1000 cm^{-1} are again consistent with the concept of Raman-active modes involving silicate-octahedral breathing motions. The more complex structure of the Raman signal in this range (Table 3) showing at least seven peaks rather than three (Caracas and Cohen 2006) indicates a symmetry reduction that may be consistent with kinked post-perovskite structures.

The larger than expected number of Raman peaks suggests a lower symmetry and larger unit cell than that of the $CaIrO_3$-type phase, not inconsistent with the 2 × 1 and the 3 × 1 structure, which have 42 and 54 Raman active modes, respectively (Kroumova et al. 2003).

The spectra from Samples 1 and 2 are similar but not identical. However, their composition and, according to our analysis

TABLE 3. Energies of the observed Raman peaks

Sample 1, 110–120 GPa, $(Mg_{1.92},Al_{0.06},Fe_{0.01})Si_{1.984}O_6$			Sample 2, 91–96 GPa, $(Mg_{1.16},Fe_{0.45},Al_{0.20},Na_{0.12})Si_{2.19}O_6$		
Number	Energy (cm^{-1})	Comment	Number	Energy (cm^{-1})	Comment
1	145	Shoulder			
2	154				
3	175				
4	252	Strong			
5	270				
6	277	?, shoulder			
7	285	Shoulder			
8	301	Weak			
9	329	Strong	1	334	
10	350	Strong	2	356	
11	360	Strong			
12	374	Strong			
13	382	Strong		399	broad, pv
14	470		3	490	shoulder, broad
			4	499	weak
15	495	? weak	5	539	
16	636	Broad		576	pv
17	675	Broad	6	656	broad, strong
18	723	broad, shoulder	7	725	weak
19	754	broad, shoulder		763	pv
20	783	shoulder, strong			
21	825	very strong			
22	870	shoulder, strong	8	866	broad, very strong
23	902	shoulder, strong			
24	966				

of the X-ray diffraction data, their structures are different also while sharing a common construction principle (Figs. 1b and 1c). Both spectra share the occurrence of Raman peaks above 800 cm^{-1}, which are not expected for perovskite (Serghiou et al. 1998; Karki et al. 2000; Caracas and Cohen 2006), but may be a signature of post-perovskite structures. The larger half width of these high-energy Raman peaks in comparison to the lower energy peaks in the same spectra may be due to disorder and to Al substitution on the Si sites, but this remains speculative as long as we are lacking definitive structure solutions for the observed phases.

In summary, our ab-initio calculations have reproduced the n × m type kinked post-perovskite structures found in metadynamics calculations by Oganov et al. (2005), and we extended our calculations to further polymorphs of this type. We have shown that kinked post-perovskites correspond to local minima in the energy hypersurface at 0 K. Above 100 GPa, the calculated enthalpy of the kinked structures is lower than that of perovskite but remains higher than that of $CaIrO_3$-type post-perovskite. Thus kinked type structures are not stable at 0 K, but they may be stabilized at high temperature due to thermal contributions to the Gibbs free energy that are neglected in our calculations. The energetic preference for the $CaIrO_3$-type at 0 K holds for pure $MgSiO_3$ as well as for charge-coupled aluminum substitutions in $MgSiO_3$. Both X-ray diffraction data and Raman spectra on aluminous magnesium metasilicate show features that are not expected for perovskite or $CaIrO_3$-type post-perovskite. Our Raman spectra show similarities with the predicted spectrum for $CaIrO_3$-type post-perovskite. However, the large number of Raman peaks suggests lower symmetry and larger unit cell size than that of $CaIrO_3$-type post-perovskite. These observations from Raman and X-ray diffraction data and the comparison to the diffraction patterns derived from our ab-initio calculations suggest that the structures in our experiments are more consistent with kinked structures of the type n × 1 than with perovskite or $CaIrO_3$-type post-perovskite.

Our calculations show that at 0 K and for pure and aluminous $MgSiO_3$, kinked structures become more stable than perovskite at Mbar pressures but remain less stable than $CaIrO_3$-type post-perovskite, consistent with previous predictions from metadynamics simulations (Oganov et al. 2005). In the absence of detailed knowledge of the activation barriers between the local minima that belong to different n × m structures, it is not possible to assess the thermal stability of the kinked structures from theory alone. Thus, it is not clear if kinked structures are stable or metastable for sufficiently long time to be relevant for the evolution of the Earth's lowermost mantle or if they are remnants of an incomplete phase transition. However, independent of the possibility of a natural occurrence of kinked post-perovskite structures in the deep mantle our results support the previous conjecture that the perovskite → post-perovskite structural transition proceeds via intermediate kinked structures rather than by homogeneously straining the perovskite structure.

ACKNOWLEDGMENTS

We thank T. Tsuchiya, R. Wentzcovitch, and A. Oganov for fruitful discussions. We thank C. Prewitt and an anonymous reviewer for providing helpful comments improving the manuscript. We gratefully acknowledge P.D. Asimow for providing the opx starting material. We thank V. Prakapenka for allowing us to use the GSECARS Raman spectrometer at APS. GSECARS is supported by the NSF-Earth Sciences, DOE-Geosciences, and the State of Illinois. This work was supported through NSF grant 0552010 and the NNSA Cooperative Agreement DE-FC88-01NV14049. Use of the HPCAT facility was supported by DOE-BES, DOE-NNSA, NSF, DOD-TACOM, and the W.M. Keck Foundation. A.P.S. is supported by DOE-BES under contract no. W-31-109-Eng-38.

REFERENCES CITED

Blöchl, P.E. (1994) Projector augmented-wave method. Physical Review B, 50, 17953–17979.

Bolfan-Casanova, N., Keppler, H., and Rubie, D.C. (2003) Water partitioning at 660 km depth and evidence for very low water solubility in magnesium silicate perovskite. Geophysical Research Letters, 30, Art. No. 1905.

Caracas, R. and Cohen, R.E. (2006) Theoretical determination of the Raman spectra of $MgSiO_3$ perovskite and post-perovskite at high pressure. Geophysical Research Letters, 33, Art. No. L12S05.

Fei, Y., Ricolleau, A., Frank, M., Mibe, K., Shen, G., and Prakapenka, V. (2007) Toward an internally consistent pressure scale. Proceedings of the National Academy of Sciences of the United States of America, 114, 9182–9184.

Hammersley, A.P., Svensson, S.O., Hanfland, M., Fitch, A.N., and Hausermann, D. (1996) Two-dimensional detector software: From real detector to idealised image or two-theta scan. High Pressure Research, 14, 235–248.
Helmberger, D., Lay, T., Ni, S., and Gurnis, M. (2005) Deep mantle structure and the postperovskite phase transition. Proceedings of the National Academy of Sciences of the United States of America, 102, 17257–17263.
Hohenberg, P. and Kohn, W. (1964) Inhomogeneous electron gas. Physical Review B, 136, 864–871.
Holzapfel, W.B. (2003) Refinement of the ruby luminescence pressure scale. Journal of Applied Physics, 93, 1813–1818.
Kameyama, M. and Yuen, D.A. (2006) 3-D convection studies on the thermal state in the lower mantle with post-perovskite phase transition. Geophysical Research Letters, 33, Art. No. L12S10.
Karki, B.B., Wentzcovitch, R.M., de Gironcoli, S., and Baroni, S. (2000) Ab initio lattice dynamics of $MgSiO_3$ perovskite at high pressure. Physical Review B, 62, 14750–14756.
Kiefer, B. and Duffy, T.S. (2005) Finite element simulations of the laser-heated diamond-anvil cell. Journal of Applied Physics, 97, 114902.
Kresse, G. and Furthmüller, J. (1996) Efficient iterative schemes for ab initio total-energy calculations using a plane wave basis set. Physical Review B, 54, 11169–11186.
Kresse, G. and Hafner, J. (1993) Ab-initio molecular-dynamics for open shell transition metals. Physical Review B, 48, 13115–13118.
Kresse, G. and Joubert, D. (1999) From ultrasoft pseudopotentials to the projector augmented-wave method. Physical Review B, 59, 1758–1775.
Kroumova, E., Aroyo, M.I., Perez-Mato, J.M., Kirov, A., Capillas, C., Ivantchev, S., and Wondratschek, H. (2003) Bilbao crystallographic server: Useful databases and tools for phase-transition studies. Phase Transitions, 76, 155–170.
Lin, J.F., Degtyareva, O., Prewitt, C.T., Dera, P., Sata, N., Gregoryanz, E., Mao, H.K., and Hemley, R.J. (2004) Crystal structure of a high-pressure/high-temperature phase of alumina by in situ X-ray diffraction. Nature Materials, 3, 389–393.
Mao, H.K., Wu, Y., Chen, L.C., Shu, J.F., and Jephcoat, A.P. (1990) Static compression of iron to 300 GPa and $Fe_{0.8}Ni_{0.2}$ alloy to 260 GPa: Implications for composition of the core. Journal of Geophysical Research, 95, 21737–21742.
Monkhorst, M.J. and Pack, J.D. (1976) Special points for Brillouin-zone integrations. Physics Reviews B, 13, 5188–5192.
Murakami, M., Hirose, K., Kawamura, K., Sata, N., and Ohishi, Y. (2004) Post-perovskite phase transition in $MgSiO_3$. Science, 304, 855–858.
Nakagawa, T. and Tackley, P.J. (2004) Effects of a perovskite-post perovskite phase change near core-mantle boundary in compressible mantle convection. Geophysical Research Letters, 31, 4–5.
Oganov, A.R. and Ono, S. (2004) Theoretical and experimental evidence for a post-perovskite phase of $MgSiO_3$ in Earth's D" layer. Nature, 430, 445–448.
Oganov, A.R., Martonak, R., Laio, A., Raiteri, P., and Parinello, M. (2005) Anisotropy of Earth's D'' layer and stacking faults in the $MgSiO_3$ post-perovskite phase. Nature, 438, 1142–1144.
Perdew, J.P., Burke, K., and Enzerhof, M. (1996) Generalized gradient approximation made simple. Physical Review Letters, 77, 3865–3868.
Ross, N.L., Gibbs, G.V., and Rosso, K.M. (2003) Potential docking sites and positions of hydrogen in high-pressure silicates. American Mineralogist, 88, 1452–1459.
Sata, N., Shen, G.Y., Rivers, M.L., and Sutton, S.R. (2002) Pressure-volume equation of state of the high-pressure B2 phase of NaCl. Physical Review B, 65, no. 104114.
Serghiou, G., Zerr, A., and Boehler, R. (1998) $(Mg,Fe)SiO_3$-perovskite stability under lower mantle conditions. Science, 280, 2093–2095.
Tateno, S., Hirose, K., Sata, N., and Ohishi, Y. (2005) Phase relations in $Mg_3Al_2Si_3O_{12}$ to 180 GPa: Effect of Al on post-perovskite phase transition. Geophysical Research Letters, 32, Art. No. L15306.
Tsuchiya, T., Tsuchiya, J., Umemoto, K., and Wentzcovitch, R.M. (2004a) Phase transition in $MgSiO_3$ perovskite in the Earth's lower mantle. Earth and Planetary Science Letters, 224, 241–248.
von Dreele, R.B. (1997) Quantitative texture analysis by Rietveld refinement. Journal of Applied Crystallography, 30, 517–525.

Manuscript received June 30, 2006
Manuscript accepted November 12, 2007
Manuscript handled by Przemyslaw Dera

Appendix

In this appendix we present diffraction data collected at 115 GPa in the third heating-loading cycle of the first experiment. Upon heating the sample recrystallized to a coarse-grained aggregate of just a few crystallites and the initial powder diffraction fringes evolved into arrays of single-crystal reflections that belong to these various crystallites. We singled out a set of reflections that appear to establish two intersecting stacks of lattice planes (Fig. 1). The 2ϑ values of these reflections are compared to calculated values of $CaIrO_3$-type post-perovskite and various kinked post-perovskites. Some $n \times 1$ type kinked phases match the observed 2ϑ values but $CaIrO_3$-type post-perovskite does not (Table 1). Even an extreme distortion of the $CaIrO_3$-type cell to a density of 5.9 g/cm³ (second set of 2θ values) does not improve the match to a satisfactory degree (Table 1).

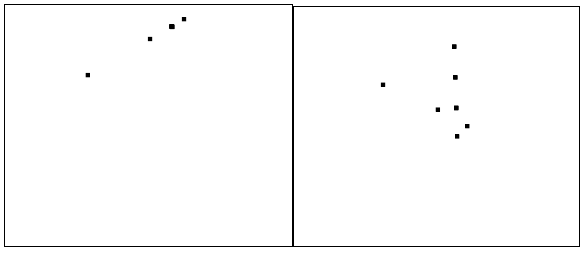

Appendix Figure 1. Correlation of observed reflections in reciprocal space. We show the array of a total of 10 reflections in two different parallel projections. The reflections establish two intersecting sequences of reciprocal lattice vectors thus spanning a two-dimensional reciprocal lattice. The observable portion of reciprocal space is essentially two-dimensional since the sample containing Mao-Bell type diamond anvil cell could not be rotated during the experiment. The two-dimensional character of the available set of reflections does not permit rigorous indexing. We, therefore, considered the 2θ angles of the observed reflections only and compared them to predicted values of perovskite, $CaIrO_3$-type post-perovskite and kinked post-perovskites as shown in Table 1.

Appendix Table 1. Comparison of observed and calculated 2ϑ angles of postperovskite-type silicate at 115 GPa

$CaIrO_3$-type*		2×1-type		3×1-type		4×1-type		Observed 2ϑ	Number of observations
hkl	2ϑ	*hkl*	2ϑ	*hkl*	2ϑ	*hkl*	2ϑ		
020	5.26/4.94								
						020	6.42	6.4	1
021	6.31/6.22	−111	6.53	−102	6.24				
002	6.94/7.57	−201	7.46	031	7.60				
		−211	8.20			021	7.77	7.73	1
022	8.72/9.04								
040	10.54/9.89	102	10.76	201	10.67	−131	10.78	10.78	2
		301	10.83			022	10.85	10.84	1
041	11.10/10.59			−212	10.96	501	10.90	10.92	1
		−113	15.42	−126	15.39	403	15.41	15.41	2
133	15.69/16.03								
060	15.84/14.85								
115	19.64/20.98								
		−602	19.95	118	19.91	−161	19.95	19.93	2
045	20.40/21.56								

* We give 2ϑ values for the ab initio calculated and a cell optimized to match observed reflections.